coatings

MDPI

*Article*

# Spectrally Selective Solar Absorber Coating of W/WAlSiN/SiON/$SiO_2$ with Enhanced Absorption through Gradation of Optical Constants: Validation by Simulation

**K. Niranjan [1,2], Paruchuri Kondaiah [1], Arup Biswas [3], V. Praveen Kumar [1], G. Srinivas [1] and Harish C. Barshilia [1,2,*]**

[1] Nanomaterials Research Laboratory, Surface Engineering Division, CSIR-National Aerospace Laboratories, Bangalore 560017, India; niru.snakes@gmail.com (K.N.); paruchurikondaiah@gmail.com (P.K.); praveenkv@nal.res.in (V.P.K.); Sree9977@nal.res.in (G.S.)
[2] Academy of Scientific and Innovative Research (AcSIR), Ghaziabad 201002, India
[3] Atomic and Molecular Physics Division, Bhabha Atomic Research Centre, Mumbai 400085, India; arup.bi@gmail.com
* Correspondence: harish@nal.res.in

**Abstract:** The properties of spectrally selective solar absorber coatings can be fine-tuned by varying the thickness and composition of the individual layers. We have deposited individual layers of WAlSiN, SiON, and $SiO_2$ of thicknesses ~940, 445, and 400 nm, respectively, for measuring the refractive indices and extinction coefficients using spectroscopic ellipsometer measurements. Appropriate dispersion models were used for curve fitting of ψ and Δ for individual and multilayer stacks in obtaining the optical constants. The W/WAlSiN/SiON/$SiO_2$ solar absorber exhibits a high solar absorptance of 0.955 and low thermal emissivity of 0.10. The refractive indices and extinction coefficients of different layers in the multilayer stack decrease from the substrate to the top anti-reflection layer. The graded refractive index of the individual layers in the multilayer stack enhances the solar absorption. In the tandem absorber, WAlSiN is the main absorbing layer, whereas SiON and $SiO_2$ act as anti-reflection layers. A commercial simulation tool was used to generate the theoretical reflectance spectra using the optical constants are in well accordance with the experimental data. We have attempted to understand the gradation in refractive indices of the multilayer stack and the physics behind it by computational simulation method in explaining the achieved optical properties. In brief, the novelty of the present work is in designing the solar absorber coating based on computational simulation and ellipsometry measurements of individual layers and multilayer stack in achieving a high solar selectivity. The superior optical properties of W/WAlSiN/SiON/$SiO_2$ makes it a potential candidate for spectrally selective solar absorber coatings.

**Keywords:** spectrally selective absorber; multilayer stack; spectroscopic ellipsometry; optical constants; simulation



**Citation:** Niranjan, K.; Kondaiah, P.; Biswas, A.; Kumar, V.P.; Srinivas, G.; Barshilia, H.C. Spectrally Selective Solar Absorber Coating of W/WAlSiN/SiON/$SiO_2$ with Enhanced Absorption through Gradation of Optical Constants: Validation by Simulation. *Coatings* **2021**, *11*, 334. https://doi.org/10.3390/coatings11030334

Academic Editor: Alicia de Andrés

Received: 6 January 2021
Accepted: 11 March 2021
Published: 15 March 2021



## 1. Introduction

Solar energy is one of the abundantly available renewable sources and has drawn researchers' interest due to diminishing non-renewable energy (fossil fuels). The solar radiation is converted into thermal energy through photothermal conversion by means of concentrated solar power (CSP) plants, which is a suitable way of producing thermal energy and disposable electricity [1]. The solar absorber has a significant role in improving the overall efficiency of CSP, as solar absorber coating determines the photothermal conversion of incident solar radiation to heat energy [2]. A real solar absorber coating should possess high solar absorptance ($\alpha \geq 0.950$) in the solar spectrum range (0.25–2.5 μm) and very low thermal emissivity ($\varepsilon \leq 0.10$) in the infrared (IR) range (2.5–25 μm) [3]. Spectrally selective solar absorbers with high solar absorptance, low thermal emissivity and high thermal stability deposited using physical vapor deposited (PVD) are widely used in

parabolic trough collectors operating at temperatures of 400 °C at maximum. In recent years, solar absorbers have drawn massive interest due to their novel optical properties in the solar spectral and IR range [4]. Solar selective coatings are broadly classified into five different types namely: (a) Intrinsic absorber, (b) semiconductor absorber, (c) textured surfaces, (d) multilayer stack, and (e) cermet-based absorbers. Amongst these, multilayer stack and cermet-based solar absorbers are widely investigated [5]. The multilayer stack and/or cermet-based solar absorber consists of an infrared reflector, an absorber and an anti-reflection layer. The metal interlayers such as W, Mo, Ni, and Ti in the multilayer stack are mainly used to reduce the thermal emissivity of the coating in the infrared region at high temperatures [6,7]. Tungsten (W) is a potential material as interlayer due to its excellent thermal stability, low infrared emissivity and also acts as diffusion barrier. In case of absorbers, a wide range of transition metal nitrides/oxynitride based solar absorber coatings have been developed due to the tuneable optical properties and high thermal stability at elevated temperatures. Transition metals like Cr, Mn, W, Ni, and Mo usually show good selectivity and good thermal stability via doping of nitrogen and oxygen to form respective nitrides, oxynitrides, and oxides as main absorber layers [8]. Various anti-reflection layers such as $SiO_2$, $SiO_xN_y$, $Si_3N_4$, $TiO_2$, $Al_2O_3$, and $AlSiO_y$ are used in solar absorbers based on the application [9–11]. The anti-reflection layer deposited on the absorber layer reduces the surface reflection and thereby reducing the reflection losses. In this regard, a multilayer stack is designed by optimizing the optical properties of individual layers to achieve high absorptance.

The optical properties of thin films are mainly dependent on the optical constants, i.e., refractive index ($n$) and extinction coefficient ($k$). The refractive index of the individual layers has a significant effect in designing a high absorptance solar selective coating. A gradation in refractive index from top anti-reflection layer to bottom of the substrate in the multilayers stack significantly increases the absorption of the coating [6]. A wide range of wavelengths in solar radiation can experience enhanced absorption due to multiple reflections at layer interfaces. Two factors are usually attributed to the absorption in thin films: One is because the phase difference between the top and bottom layers of the coating surface accounts for destructive interference of light and the other is band-to-band transitions. The refractive indices and extinction coefficients of the individual layers in the multi-layer stack determine the reflectance behavior, thereby, helping in better under-standing of the absorption mechanism and high solar selectivity ($\alpha/\varepsilon$). In the past decade, several reports have been devoted on the effect of refractive index and extinction coefficient on the optical properties [12–16]. The refractive index and extinction coefficient of each layer is broadly interpreted with spectroscopic ellipsometry measurements. Biswas et al. reported the ellipsometry studies of $TiAlN/TiAlON/Si_3N_4$ tandem absorber deposited on Cu substrate. They correlated the measured ellipsometry spectra with theoretical simulated spectra based on the optical constant determined for each layer [17]. Dan et al. reported the optical constants of $W/WAlN/WAlON/Al_2O_3$ multilayer coating with the presence of intermixed layers between WAlN and WAlON based on ellipsometry studies. The simulation using these optical constants indicates good correlation between the simulated and experimental measured reflectance spectra [18]. Similarly, Al-Rjoub et al. reported the optical constants of $WAlSiN_x$, $WAlSiO_yN_x$, and $SiAlO_y$ layers by varying the nitrogen and oxygen partial pressures. The multilayer stack was designed based on obtained optical constants using simulation software which exhibited a high solar absorptance of 0.96 and low thermal emissivity of 0.105 (calculated $\varepsilon_{400\,^\circ C}$) [19]. Yet in another work, Escobar-Galindo et al. reported $Al_yTi_{1-y}(O_xN_{1-x})$ based solar absorber multilayer coatings, which are stable up to 650 °C for 12 h and the simulated results are in good accordance with the experimental reflectance data [20]. Similarly, Wang et al. reported an aperiodic metal-dielectric multilayer based on AlCrN and AlCrON high-temperature stable coating (500 °C for 1000 h) with high solar selectivity ($\alpha/\varepsilon$) of 0.94/0.11 [21]. In this regard, a wide range of solar selective coatings developed by several groups are: Cu/TiAlCrN/TiAlN/AlSiN [22], $MoSi_2$–$SiO_2$ [23], AlCrSiN/AlCrSiON/AlCrO [24], Al/NbMoN/NbMoON/SiO2 [25], TiN/nano-multilayered

AlCrSiO/amorphous AlCrSiO [26], and W/AlSiTi$N_x$/SiAlTi$O_y N_x$/Si$AlO_x$ [27].The optical design of the coating based on optical constants, layer thickness and composition plays a major role in developing a spectrally selective absorber coating with high solar absorptance and low thermal emissivity.

In our previous work, we have demonstrated the in-depth effect of process parameters affecting the optical properties of individual layers as well as the multilayer stack of W/WAlSiN/SiON/$SiO_2$ [28]. In this manuscript, we had presented the effect of reactive gas flow rates, sputtering power, deposition time and thicknesses of individual layers to achieve high spectral selectivity. A very low reflectance (R < 5%) was observed in the wavelength range of 450–1500 nm and very high reflectance (R > 95%) in the IR region, resulting in high solar absorptance ($\alpha$ = 0.955) and low thermal emissivity ($\varepsilon$ = 0.10 @ 82°C). In another study, the thermal stability of the optimized multilayer stack has been investigated in vacuum (700 °C for 200 h) and air (400 °C for 500 h and 500 °C for 100 h) for longer duration under cyclic heating conditions. Further, the high-temperature emissivity measurements have been carried out in the temperature range of 80 °C to 460 °C and the optimized sample exhibited a thermal emissivity of 0.15 @ 460 °C [29]. The proposed multilayer stack is a potential candidate as absorber coating on receiver tubes of parabolic through collector.

One of the biggest problems for central receiver tubes used in CSP is to improve the operating temperature of solar absorber coatings to enhance the overall photo-thermal conversion efficiency. In the literature, very few coatings are reported with good thermal stability (air) in the temperature range of 400–500 °C operating for long duration [20,23,27–30]. Because of high optical absorption along with low thermal emissivity as well as enhanced thermal stability of the tandem absorber of W/WAlSiN/SiON/$SiO_2$ owing to its unique nano-multilayer design, it is important to investigate the optical constants (*n* and *k*) of individual layers as well as tandem absorber. Therefore, in this manuscript, we report the phase-modulated spectroscopic ellipsometry measurements of individual layers of WAlSiN, SiON and $SiO_2$ and multilayer stack of W/WAlSiN/SiON/$SiO_2$ for their optical constants. The optical properties of thick individual layers were measured using UV-Vis spectroscopy and the effect of surface roughness on thermal emissivity was verified. The obtained refractive indices and extinction coefficients of individual layers and multilayers stack are curve fitted using suitable dispersion medium theories. The wide-angle absorptance was investigated by varying the incident angle in the UV-Vis-NIR region from 8° to 68°. The simulated reflectance spectra using obtained optical constants of the individual layers and multilayer stack are in good agreement with the experimentally measured reflectance spectra with minimal deviation.

## 2. Experimental Details

Spectrally selective coatings of W/WAlSiN/SiON/$SiO_2$ were deposited on stainless steel (SS) and silicon (Si) substrates by a Reactive Unbalanced Direct Current (DC) Magnetron Sputtering System with high purity (>99.9%) targets of W, Al, and Si. The substrate and targets were maintained at a constant distance of 10 cm throughout the deposition. Pulsed DC power supplies were used to deposit W, WAlSiN, SiON, and $SiO_2$ layers. The reactive sputtering of W, Al, Si targets in suitable Ar, $N_2$, and $O_2$ environments for depositing the multilayer stack and individual layers. All the coatings were deposited at a substrate temperature of 200 °C and in-situ Argon (Ar) plasma cleaning for 5 min at a voltage of −1000 V. The optimized process parameters (such as: Power density, reactive gas flow rates, bias voltage, and deposition time) were used to deposit each layers as discussed in our previous paper [28].

The refractive index (*n*) and the extinction coefficient (*k*) of the multilayer stack were measured by the phase-modulated spectroscopic ellipsometry (Model UVISEL 460, ISA Jobin-Yvon-Spex, Palaiseau, France) in the wavelength range of 300–900 nm. The obtained data were further analyzed by fitting with the appropriate dispersion models. Solar absorptance and emissivity of the as-deposited samples were measured using Solar Spectrum Reflectometer (Model SSR) and Emissometer (Model AE) (Devices & Services Company,

Texas, TX, USA) of Devices and Services. The emissivity was measured at a temperature of 82 °C. The reflectance spectra of the as-deposited samples were measured in the wavelength range of 0.25–2.5 μm using UV-VIS-NIR spectrophotometer (PerkinElmer: Lambda 950, (PerkinElmer, Massachusetts, MA, USA). Fourier transform infrared spectroscopy (PerkinElmer, Massachusetts, MA, USA) was used for measuring the reflectance from NIR to MIR (2–25 μm). Cross-sectional studies of the individual layers were carried out using field-emission scanning electron microscopy (FESEM, Carl Zeiss, SUPRA 40VP, Oberkochen, Germany). The cross-sectional FESEM images of individual layers were measured using secondary electron detection mode (SE) and at an acceleration voltage of 10 kV. The thicknesses of the individual layers were measured using a 3D profilometer, Nano Map500LS (AEP Technologies, California, CA, USA). A commercial simulation tool (SCOUT Version 2.99) was used for simulating the reflectance spectra of each layers of the tandem absorber using obtained optical constants and compared with the measured reflectance spectra [31].

## 3. Results and Discussion

### *3.1. Optical Properties of Individual Layers*

The optical properties of individual layers in the multilayer stack enabled us to understand the spectral selectivity of the W/WAlSiN/SiON/$SiO_2$ solar absorber coatings. To obtain the individual layer optical properties, we have deposited the layers of WAlSiN, SiON and $SiO_2$ for long durations on SS and Si substrates. Their optical properties were measured in the wavelength range from 250–2500 nm using UV-Vis-NIR spectrophotometer. The thickness and average roughness of the film were measured from the Si substrate. The individual layer thicknesses were: 940, 445, and 400 nm for WAlSiN, SiON and $SiO_2$ layers, respectively, as labelled in insets of Figure 1. The layer thickness was measured using cross-section FESEM images as shown in the insets of Figure 1 and verified from 3D profilometer data. It is to be noted that the optical properties of W metal such as reflectance and refractive indices are well reported in the literature, therefore, the detailed characterization of W interlayer has not been carried out to avoid duplications. Figure 1a shows the reflectance spectrum of WAlSiN layer, wherein it is observed that the overall reflectance of the film is less than 40% in the UV-Vis-NIR region, indicating its absorbing nature. The layer has good absorption in UV-Vis-NIR region and we observe the interference fringes in near-IR region due constructive and destructive interference in the film. Similarly, the reflectance spectra of SiON and $SiO_2$ anti-reflection layers are as shown in Figure 1b,c with cross-section FESEM images of the coatings. However, the high reflectance of the SiON and $SiO_2$ layers indicates their non-absorbing nature. The SiON and $SiO_2$ layers are transparent in visible and near infrared region and acts as an excellent anti-reflection layers [32]. Moreover, the fringes observed in the UV-Vis region of reflectance spectra are due to interferences owing to the fact that light gets partially reflected from the substrate as these layers are transparent in this wavelength range.

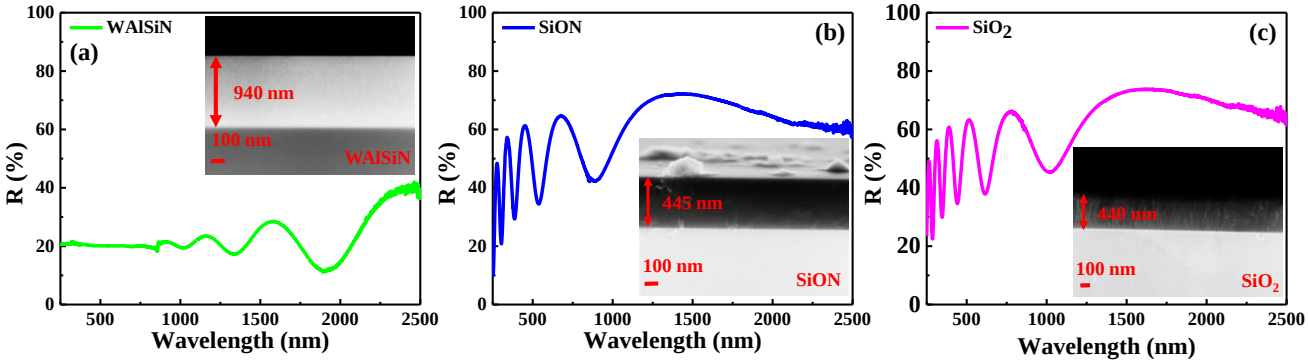


**Figure 1.** Reflectance spectra of individual layers deposited on stainless steel (SS) substrate (**a**) WAlSiN, (**b**) SiON, and (**c**) $SiO_2$. The cross-sectional FESEM images of the individual layers are shown in the insets.

The thermal emissivity depends on the material property and surface roughness of the coating. The coatings high surface roughness would considerably increase the thermal emissivity. The statement mentioned above has been proved theoretically and experimentally by various research groups [33]. The theoretical expression which correlates the dependence of thermal emissivity, surface roughness and reflectance of the coating is as in Equation (1):

$$R_r = R_p \exp\left\{-\left(\frac{4\pi\sigma}{\lambda}\right)^2\right\} \quad (1)$$

where $R_r$, $R_p$, σ and λ are reflectance of rough surface, reflectance of polished surfaces, root mean square roughness and wavelength, respectively. According to Kirchhoff's law, the emissivity and reflectance can be related using the following equation: $\varepsilon_\lambda = 1 - R_\lambda$ [34,35]. From the above two equations it is evident that with increasing surface roughness, the emissivity of the film increases [7]. However, a fine nanostructure formed on the coating surface will enhance the light absorption by multiple reflections due to light trapping [36]. Cao et al. numerically investigated the dependence of surface roughness of the film on the reflectance and thermal emissivity [37]. Similarly, Wen et al. reported the modelling of surface roughness of aluminum alloy by different theoretical models and results indicate a clear correlation between the surface roughness and thermal emissivity [38]. Recently, metal–liquid–crystal–metal (MLCM) based metasurface of Au/LC/Au are reported for their enhanced thermal camouflage by structuring the surface emissivity and optimizing the surface microstructure [39,40]. In this regard, we carried out AFM studies to evaluate the effect on optical properties based on surface roughness of individual layers and multilayer stack, as shown in Figure 2. The main absorber layer (WAlSiN, layer thickness ~940 nm) exhibited the average roughness ($R_a$) of 1.87 nm, as shown in Figure 2a and the layer exhibits a selectivity (α/ε) of 0.80/0.63. However, SiON and $SiO_2$ depicted low average roughness values of 1.31 and 1.16 nm, as shown in Figure 2b,c. The anti-reflection layers exhibit almost similar selectivity of 0.440/0.20 and 0.428/0.20 for SiON (layer thickness ~445 nm) and $SiO_2$ (layer thickness ~400 nm), respectively. The multilayer stack of W/WAlSiN/SiON/$SiO_2$ deposited on SS substrates depicts a low surface roughness of 0.61 nm and exhibits good spectral selectivity (α/ε) of 0.955/0.10. The results indicate that the surface roughness of the thin films influences the thermal emissivity of the coatings.

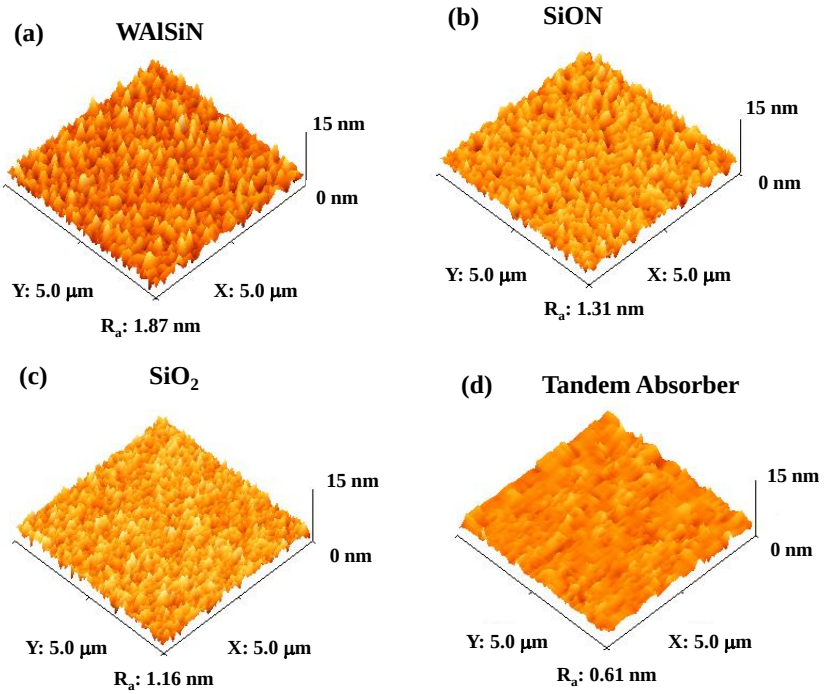


**Figure 2.** 3-dimensional AFM images of (**a**) WAlSiN, (**b**) SiON, (**c**) $SiO_2$, and (**d**) multilayer stack deposited on SS substrates.

### *3.2. Spectroscopy Ellipsometry Measurements*

#### 3.2.1. Optical Constants of Individual Layers

The solar selective properties of each layer were examined for a better understanding of optical properties. The individual layers of WAlSiN, SiON, and $SiO_2$ are deposited for measuring the optical constants using phase-modulated spectroscopic ellipsometry. In spectroscopic ellipsometry, it measures the change in the monochromatic light's polarization state reflected from the sample surface. The variations are represented as a function of ψ and Δ of the individual layers, which represents the amplitude ratio of *s* and *p* polarized light and their phase change, respectively. ψ and Δ can be represented in a complex reflection ratio ($\rho$), which is defined as the ratio of Fresnel reflection coefficient for *s* and *p* polarized light [17,41].

$$\rho = \frac{r_p}{r_s} = tan\psi \exp(i\Delta) \quad (2)$$

where, $r_p$ and $r_s$ are the reflection coefficient of *p* and *s* component of the electric field, respectively [17,18,41].

The obtained ψ and Δ data from ellipsometry are curve fitted by assuming a physical model appropriate for each layer. Theoretical simulated spectra consider a suitable optical dispersion medium for the layers. However, ψ and Δ data from ellipsometry measurements are derived from experiments and are curve fitted with an optical dispersion model for optical constant of individual layers. Some of the assumptions, considered during the fitting of experimentally obtained data with the theoretically generated data are [38]:

- The individual layer deposited are considered as homogenous model of thin-film and is simulated with a theoretical dispersion model to generate optical constants.
- The optical constants of the bare substrate are measured to attain more realistic results, and these results were compiled for curve fittings.

The optical constants are determined by considering a physical model that matches the sample and generates a generally suitable optical dispersion oscillator. In this regard, Cauchy's absorbent dispersion model was considered for WAlSiN main absorber layer,

as this layer act as absorbing layer in the multilayer stack [17,18,42]. The relations for Cauchy's absorbent dispersion medium are as shown in Equations (3) and (4):

$$n(\lambda) = A + \frac{B}{\lambda^2} + \frac{C}{\lambda^4} \tag{3}$$

$$k(\lambda) = D + \frac{E}{\lambda^2} + \frac{F}{\lambda^4} \tag{4}$$

where, $\lambda$ is the wavelength and $A$, $B$, $C$, $D$, $E$, and $F$ are fit parameters. The above equation mentions that $A$, $B$, and $C$ corresponds to the long-wavelength asymptotic refractive index value, slope and amplitude, respectively of refractive index curve, a similar notation for $D$, $E$, and $F$ [17,18]. The top SiON and $SiO_2$ layers were curve fitted with the Tauc–Lorentz (TL) oscillator model. TL model is effective for nanocrystalline and amorphous thin films [18,43]. The complex dielectric functions can be expressed in a simple oscillator model and the expression for $\varepsilon_2$ is as shown in the Equation (5):

$$\varepsilon_2 = \frac{AE_o\Gamma\left(E - E_g\right)^2}{\left[\left(E - E_g\right)^2 + \Gamma^2E^2\right]^2}\frac{1}{E};\ E > E_g \tag{5}$$

$$\varepsilon_2 = 0\ ;\ E < E_g$$

where, $E_o$, $E_g$, $\Gamma$ and $A$ are the peak transition energy, optical band gap energy, broadening parameter, and optical transition matrix elements, respectively [20,44]. From Kramers–Krönig transformation (KKT) the real part ($\varepsilon_1$) of the dielectric function is expressed as depicted in Equation (6):

$$\varepsilon_1 = \varepsilon_{\alpha,UV} + \frac{2}{\pi}P\int_{E_b}^{\alpha}\frac{\xi\varepsilon_2(\xi)}{\xi^2 - E^2}d\xi \tag{6}$$

where, $\varepsilon_{\alpha,UV}$, $\xi$ and $P$ represents the high frequency dielectric constant, linear dielectric susceptibility and principal values of the integrals, respectively [45].

Using the above dispersion models ψ and Δ data of WAlSiN, SiON and $SiO_2$ samples were curve fitted using a minimization process. This minimization process has a maximum of 100 iterations and the basis of convergence is 0.000001 ($\chi^2$ minimization—which defines the good fitting of curves). The model parameters are varied by a regression analysis until the calculated and experimental data are as close as possible. The following average square error function is minimized by weighing it to the approximate experimental errors.

$$\chi = \left\{\frac{1}{2N - M}\sum_{i=1}^{N}\left[\left(\frac{\psi_i^{mod} - \psi_i^{expt}}{\sigma_\psi^{expt},\ i}\right)^2 + \left(\frac{\Delta_i^{mod} - \Delta_i^{expt}}{\sigma_\Delta^{expt},\ i}\right)^2\right]\right\}^{\frac{1}{2}} \tag{7}$$

where, $N$, $M$, and $\sigma$ are the number of measured ψ and Δ pairs, number of variable parameters and standard deviation, respectively. The superscripts "mod" and "expt" mean the theoretical calculations and experimental data [18,46]. The curve fitted ψ and Δ of individual layers are shown by lines, which are in good accordance with the measured data, represented by symbols in Figure 3. However, the oscillations observed in SiON and $SiO_2$ in the wavelength range of 300–900 nm, due to interference as shown in Figure 3b,c. In contrast, the absence of such oscillations for the WAlSiN layer, as depicted in Figure 3a, indicates a strongly absorbing property [19]. The optical behavior of such absorbing thin films can be observed from the reflectance spectra shown in Figure 1. It is to be noted that the WAlSiN layer contains fine nano-multilayers of $W_2N$ and AlSiN, a total of 36 layers (18 layers each) as reported previously [29]. However, during the ellipsometry fitting we have considered the nano-multilayer structure of $W_2N$ ($t$ ~1.5 nm, polycrystalline phase) and AlSiN ($t$ ~3 nm, amorphous phase) as a single composite layer of WAlSiN and effective

optical constants of WAlSiN layer are obtained. This is assumed as the individual layer thickness (~3 nm) is very small compared to the measurement wavelength (300–900 nm) of the ellipsometry. The best fitted optical constant o are plotted as a function of wavelength, which are shown in Figure 4a. In the case of, WAlSiN layer the refractive index increases with wavelength, thereby making this layer ideal a material for selective absorption of solar radiation, as depicted in Figure 4a. The refractive indices of SiON and $SiO_2$ decrease with increasing wavelength, but the change is minimal throughout the wavelength range, as shown in Figure 4b,c. The decrease of the extinction coefficient ($k$) in WAlSiN film indicates the presence of interband transitions and metallic nature of the film. The "$k$" values of SiON and $SiO_2$ are zero as expected for dielectric materials. The excellent optical behavior of SiON and $SiO_2$ makes them a potential candidate for anti-reflection layers. The optical constants ($n$ and $k$) of the individual layers were calculated using different dispersion models, discussed above.

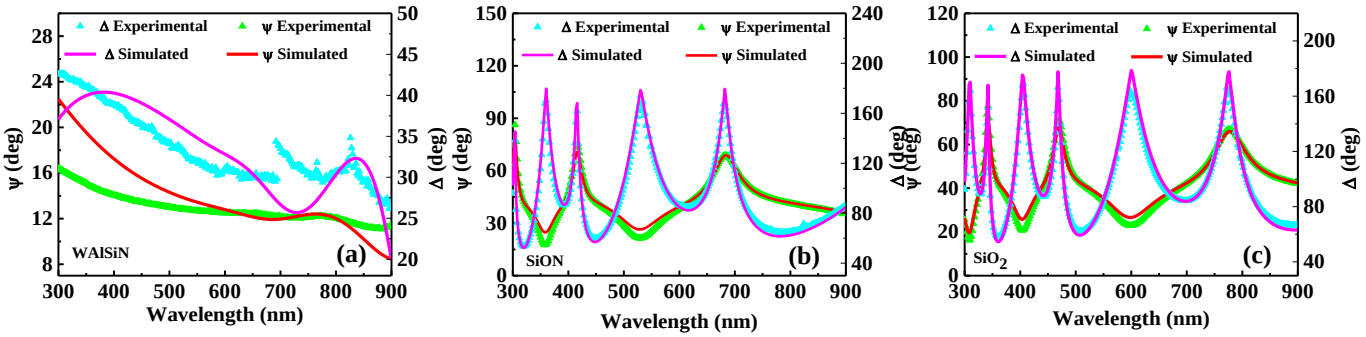


**Figure 3.** Ellipsometry spectra of individual layers, (**a**) WAlSiN, (**b**) SiON, and (**c**) $SiO_2$ deposited on SS substrate.

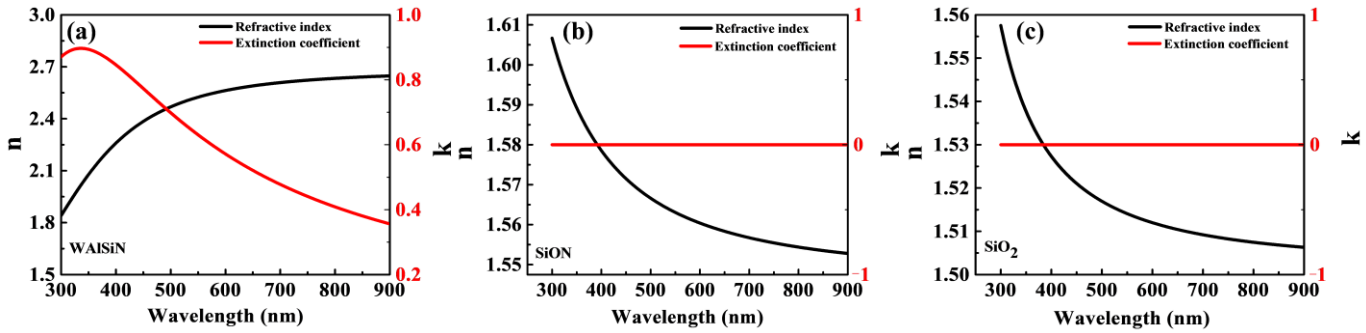


**Figure 4.** Refractive indices and extinction coefficients of individual layers (**a**) WAlSiN, (**b**) SiON, and (**c**) $SiO_2$ deposited on SS substrate.

The absorption coefficient of a material determines the depth of penetration of solar radiation into the material. It is well known that the extinction coefficient of a material is directly proportional to the optical absorption coefficient, which is as shown in the below equation:

$$\alpha = \frac{4\pi k}{\lambda} \quad (8)$$

where, $\alpha$, $k$, and $\lambda$ are absorption coefficient, extinction coefficient and wavelength [41]. The absorption coefficients calculated for individual layers using the obtained extinction coefficient are shown in Figure 5a. The higher absorption coefficient of the WAlSiN layer indicates it absorbs the incident solar radiation efficiently compared to that of SiON and $SiO_2$. Similarly, penetration depth indicates the extent to which the incident radiation penetrates inside the film thickness and the same for WAlSiN layer is shown in Figure 5b. For the WAlSiN layer with increasing wavelength, the penetration depth increases, indicating good absorption property of the layer. In contrast, SiON and $SiO_2$ films are transparent in the wavelength range of 300–900 nm.

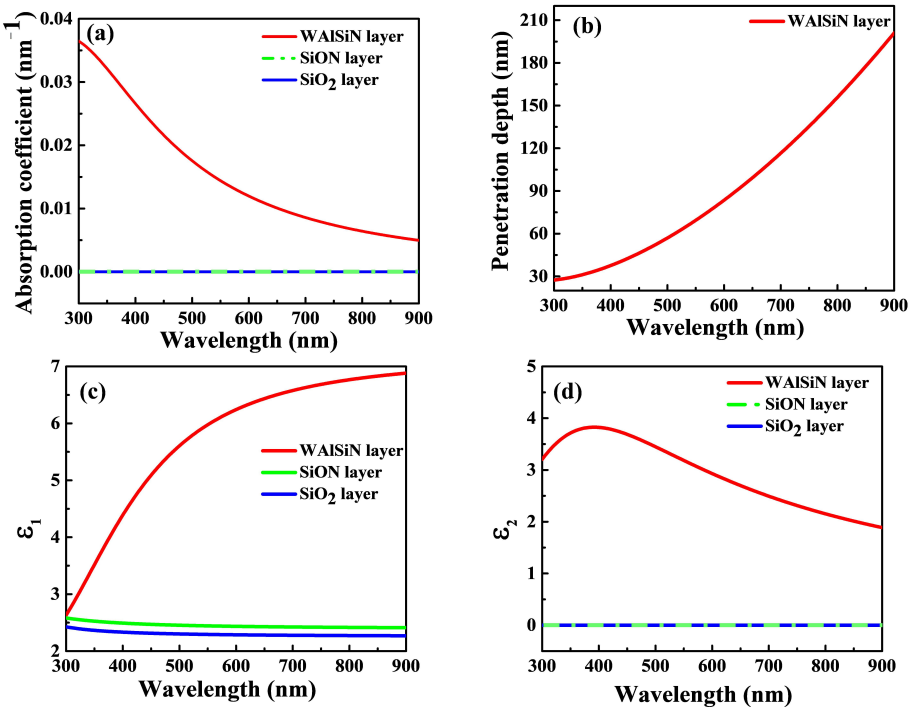


**Figure 5.** (**a**) Absorption coefficient, (**b**) penetration depth, (**c**) real ($\varepsilon_1$), and (**d**) imaginary ($\varepsilon_2$) part of the dielectric constants as a function of wavelength for single layer coatings deposited on SS substrate.

The optical properties of thin films are influenced by various material properties such as dielectric constant ($\varepsilon$), dielectric susceptibility ($\chi$), and conductivity ($\sigma$), which are treated as scalars for isotropic materials. Moreover, semiconductors and dielectric films are considered nonmagnetic and do not possess excess electrons other than the electrons bound in atoms. The relation between the optical constants ($n$ and $k$) for dielectric and semiconductor materials can be calculated from the following relations:

$$N = n + ik \text{ and } \varepsilon = \varepsilon_1 + i\,\varepsilon_2 \quad (9)$$

where, $N$ and $\varepsilon$ are complex refractive index and complex dielectric constant, respectively. Similarly, the real and imaginary part of dielectric constant can be calculated using $\varepsilon_1 = n^2 - k^2$ and $\varepsilon_2 = 2nk$, respectively [41]. The real ($\varepsilon_1$) and imaginary ($\varepsilon_2$) part of dielectric constants of individual layers were plotted using the obtained optical constants ($n$ and $k$), which are shown in Figure 5c,d. The imaginary part ($\varepsilon_2$) of dielectric constant is related to the conductivity of the material and higher ($\varepsilon_2$) indicates good conductivity due to metallic nature of the film. The $\varepsilon_1$ is related to the polarization and $\varepsilon_2$ is related to dissipation, which accounts for wide-angle selectivity and better absorption in the film, respectively. The $\varepsilon_2$ for WAlSiN layers increases with wavelength, depicting excellent absorption property of the film. However, SiON and $SiO_2$ demonstrate no absorption and are highly transparent films in the wavelength range [47,48].

### 3.2.2. Optical Constants of Multilayer Stack

The optical properties of the optimized multilayer stack were designed based on gradation in optical constants of each layers calculated using the dispersion theories. The metal W is well explored and reported in the literature as a material with high refractive index of 3.83 and good IR reflector [49]. Moreover, the sole purpose of the W interlayer is to reduce the overall thermal emissivity of the coating and acts as a diffusion barrier at high temperature. The experimentally measured optical constants of individual layers were

fitted for W/WAlSiN/SiON/$SiO_2$ with multilayer model. By considering this we account the overall optical behavior of the layers in the stack as well as the effect of each individual layers in achieving high solar selectivity ($\alpha/\varepsilon$). The curve fitted $\psi$ and $\Delta$ of the multilayer stack are shown in solid lines and which are in good accordance with the measured data, as shown in Figure 6a. The best curve fitting of the multilayer stack shown in Figure 6a emphasizes that the assumption of considering the nano-multilayers of $W_2N$ and AlSiN layers present in WAlSiN main absorber layer, which is considered as a single composite layer, has insignificant impact on the calculated optical constants. The experimental fitting of the multilayer stack depicts the presence of intermixed layer in between WAlSiN and SiON layer. The optical constants of intermixed layer were evaluated using Bruggeman effective-medium approximation (EMA) [18,50,51]. The EMA model is sensitive to the surface roughness of the layers, but the intermixed layer thickness is ~5 nm and the surface roughness can be neglected. The intermixed layer formed at the interface of WAlSiN and SiON layer has to be better understood for its influence over the optical properties of the multilayer stack. The multilayer stacks optical constants with gradation in the refractive index and extinction coefficient are drawn as a function of wavelength and is as shown in Figure 6b,c. The refractive indices of W, WAlSiN, intermixed layer, SiON and $SiO_2$ in the multilayer stack measured at 550 nm are 3.83, 2.52, 2.28, 1.56, and 1.51, respectively, as shown in the inset of Figure 6b. The lower refractive index of SiON and $SiO_2$ layers shows the dielectric nature of the films. The trend of refractive index in the multilayer stack depicts an increase from top anti-reflection layers to the substrate. At each interface of the layers, the incident solar radiation will change the phase by 180°, leading to maximum absorption of light [52]. This graded refractive index concept is well reported and is an efficient way in trapping light and in achieving enhanced solar absorption of the multilayer coatings as explained in the below section [53–55].

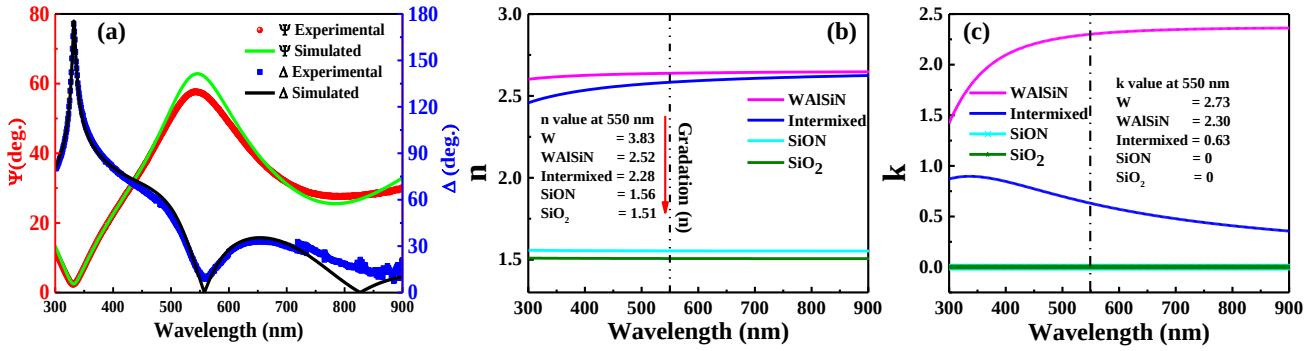


**Figure 6.** (**a**) Ellipsometry spectra of solar absorber coating, (**b**) refractive index and (**c**) extinction coefficient of WAlSiN/SiON/$SiO_2$ multilayer stack deposited on SS substrate. The refractive index and extinction coefficient of W are depicted in (**b**) and (**c**).

### *3.3. Optical Properties of Multilayer Stack*

To understand the behavior of high solar absorptance of the multilayer stack, we have deposited successive layers step by step (SS, SS/W, SS/W/WAlSiN, SS/W/WAlSiN/SiON, and SS/W/WAlSiN/SiON/$SiO_2$) and measured the reflectance spectra of each sample. From the reflectance spectra it clear that by addition of one more layer on the top, the reflectance in the UV-Vis region reduces and near-zero reflectance is achieved after deposition of last layer, as shown in Figure 7. We have measured the reflectance of polished SS substrate as a reference of reflectance for characterization of layers deposited on it successively and the optical properties ($\alpha$ and $\varepsilon$) are tabulated in Table 1. The deposition of the WAlSiN layer with fine-nano multilayers over the W interlayer results in a significant drop of reflectance in the UV-Vis region due to interference, as seen in Figure 7. Further, adding of SiON and $SiO_2$ anti-reflection layers the reflectance to near zero in the wavelength range

of 500–1300 nm is achieved due to gradation in refractive indices of the layers as shown in Figure 6 [56].

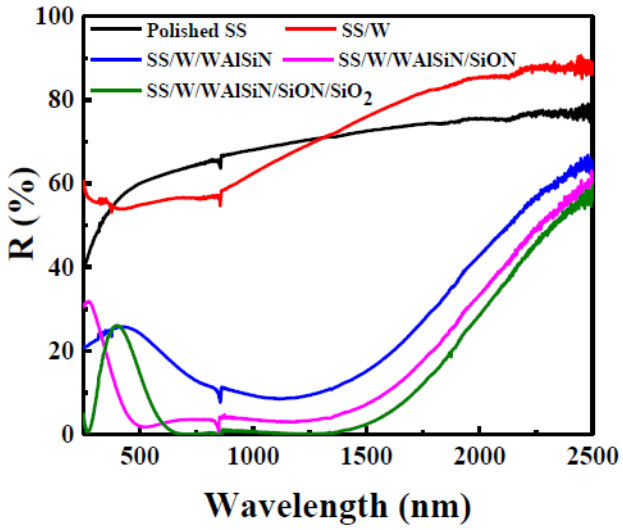


**Figure 7.** The reflectance spectra of successive layer-by-layer deposited on SS substrate.

**Table 1.** Solar absorptance and thermal emissivity of layer-by-layer deposited on SS substrate.

| Sl. No | Description | Solar Absorptance (α) | Thermal Emissivity (ε) |
|---|---|---|---|
| 1 | SS | 0.320 | 0.13 |
| 2 | SS/W | 0.40 | 0.08 |
| 3 | SS/WAlSiN | 0.850 | 0.12 |
| 4 | SS/WAlSiN/SiON | 0.950 | 0.11 |
| 5 | SS/WAlSiN/SiON/$SiO_2$ | 0.955 | 0.10 |

The schematic representation of the multilayer tandem stack of W/WAlSiN/SiON/$SiO_2$ deposited on the SS substrate, as shown in Figure 8a. The schematic depicts an intermixed layer between WAlSiN and SiON layer, a detailed explanation of this is mentioned in the below section. The thicknesses of each individual layers in the multilayer stack are labelled in the schematic, as depicted in Figure 8a. The selective solar absorber coating is designed based on a graded refractive index with a double anti-reflection layer. The reflectance spectra of the multilayer stack are as shown in Figure 8b, exhibits near-zero reflectance in the wavelength range of 0.6–1.4 μm and high reflectance of above 90% in the infrared region [28]. The low reflectance and high absorptance in the multilayer stack is due to destructive interference and band-to-band transitions [3]. A graded design of a multilayer stack generates a step-by-step change in the refractive index, resulting in lower reflection due to interference effect. Additionally, the double anti-reflection layer (DLAR) of SiON/$SiO_2$ reduces the reflection losses at the surface and enhances the absorption by trapping the incident solar radiation [10,32,57]. Kim et al. reported the DLAR coatings of $SiN_x$/$SiO_2$ of different thicknesses and the refractive indices of each layer were theoretically calculated using Essential Macleod software. They also reported that DLAR coatings exhibited better solar efficiency when compared to single $SiN_x$ anti-reflection layer [10]. Moreover, the absorption of light over a wide range of wavelength is achieved better in DLAR than a single ARC layer [58]. In summary, we have demonstrated that the gradient in the refractive index of the individual layers in the multilayer stack responsible for the enhanced absorption (high α).

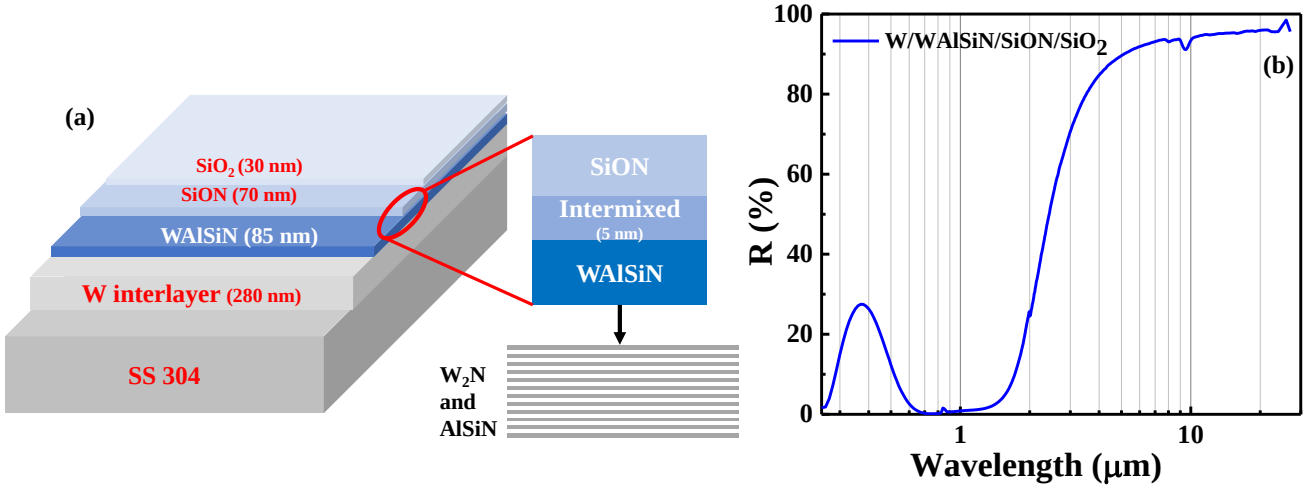


**Figure 8.** (**a**) Schematic of the multilayer stack deposited on SS substrate and (**b**) The reflectance spectrum of the optimized sample of the multilayer stack [28].

### *3.4. Angular Dependence of Solar Absorptance*

The angle of incidence of solar radiation on the multilayer stack has direct influence over the reflectance and overall performance of the system. By varying the angle of incidence, the reflectance spectra are measured for the multilayer stack using UV-Vis-NIR spectrophotometer. The influence on optical properties of the multilayer stack with change in incident angle was studied in detail. The incident angle was varied from 8°–68° and the transverse electric (TE), i.e., *s* polarization and transverse magnetic (TM), i.e., p polarization reflectance spectra were recorded as a function of wavelength, as shown in Figure 9. The *p* polarization reflectance spectra ($R_p$) depict a decrease in reflectance up to an incident angle of 58° and further it increases at 68° incident angle, as shown in Figure 9a. The reflectance of the multilayer stack is less than 6% in the wavelength range of 500–1500 nm, which indicates good selectivity as well as wide angle solar absorptance. Similarly, the *s* polarization reflectance spectra ($R_s$) show an increase in reflectance of the film with increasing incident angle, as shown in Figure 9b. A slight shift in reflectance minima towards shorter wavelength is observed in reflectance spectra form 38°–68°. This is due the fact that at higher incident angles the effective thickness of the coating interacting with light is thinner compared to the actual thickness [59]. However, the average reflectance spectra of *s* and *p* polarization indicate a low reflectance (less than 10%) with varying incident angle, as shown in Figure 9c. These results demonstrate excellent wide-angle solar selectivity of W/WAlSiN/SiON/$SiO_2$ multilayer stack up to 58°.

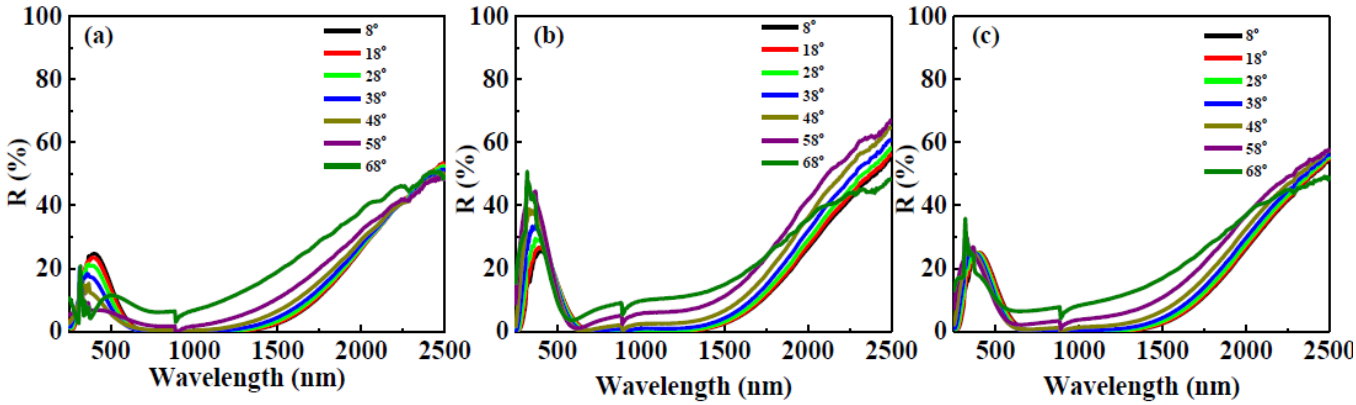


**Figure 9.** Angular absolute reflectance studies of the multilayer stack in UV-Vis-NIR region (**a**) TM polarization ($R_p$), (**b**) TE polarization ($R_s$), and (**c**) Average reflectance R = ($R_p$ + $R_s$)/2.

### *3.5. Optical Simulation of Individual Layers and Multilayer Stack*

A commercial simulation tool is used for determining the calculated reflectance spectra based on optical constants of the materials and film thicknesses [31]. The design of the solar absorber coating of W/WAlSiN/SiON/$SiO_2$ was carried out using simulation to minimize the number of experiments. The simulation was carried out to reduce the reflectance in the UV-ViS-NIR region by varying the refractive indices and thicknesses of the individual layers in the multilayer stack. Subsequently, the simulated reflectance data of the designed solar absorber coating was compared with the actual deposited W/WAlSiN/SiON/$SiO_2$ coating and similar approach was used for individual layers (WAlSiN, SiON and $SiO_2$) as well. The computational studies of WAlSiN, SiON, and $SiO_2$ layers were based on the optical constants obtained using spectroscopy ellipsometry and the reflectance spectra is generated in the wavelength range of 300–2500 nm. The refractive index ($n$) and extinction coefficient ($k$) of each individual layer are used for the simulation. Reference was inputted from experimentally measured reflectance spectra. The deviation was computed as a simple mean squared difference. Individual points on the simulated and imported reflectance spectra were compared and deviation was computed. The displayed value is the average of mean squared values over the defined range. The simulation fitting between the simulated and the measured spectra is evaluated using the deviation value. The simulation fitting is described as rejected, bad, acceptable, good and excellent based on the fit deviation value i.e., 0.1, 0.01, 0.001, 0.0001, and 0.00001, respectively [31]. The fit deviation values of all the simulated spectra are tabulated in Table 2 and a low deviation value indicates good and excellent fits of the simulated spectra. The simulated and experimental spectra of WAlSiN, SiON, and $SiO_2$ thick individual layers (Figure 10a–c and the deviations of the fit are tabulated in Table 2. The optical constants are acquired from ellipsometry studies of the individual layers as well as the multilayer stack, as discussed above. The data fitting in simulation software of the individual layers showed a deviation, which is attributed to available ellipsometry data of the individual layers in the limited wavelength range (300–900 nm). The deviation between the two spectra exists for various reasons. The most important one being the range over which ellipsometry data was collected. Ellipsometry data is collected up to 900 nm, while reflectance data is plotted up to 2500 nm. The simulation tool assumes a constant value ($n$, $k$ at 900 nm) of the ellipsometry data in 900–2500 (missing data range). This can be justified as the fitting for the particular layer thickness well matched with the experimentally measured reflectance spectra in the range of 300–900 nm. These measurement errors influence a minor deviation in the reflectance spectra generated through SCOUT simulation software to that of the experimentally measured reflectance spectra. The fit deviations are tabulated in Table 2. However, the effective optical constant of WAlSiN layer used for simulation indicates an excellent fit, which implies that the calculated optical constants of WAlSiN layer are accurate.

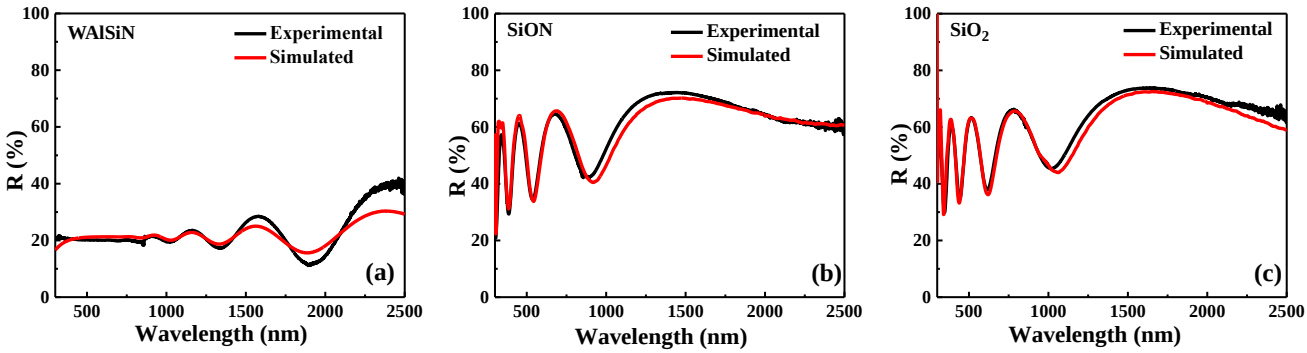


**Figure 10.** Experimental reflectance spectra of the individual layers in the tandem stack fitted with the simulated spectra obtained from SCOUT simulation software (**a**) WAlSiN, (**b**) SiON, and (**c**) $SiO_2$ layer.

**Table 2.** Thicknesses of the individual layers and tandem absorber used to generate the simulated reflectance spectra, fit deviation with experimentally measured spectra.

| Sl. No | Description | Layer Thickness (nm) | | Deviation |
|---|---|---|---|---|
| | | Experimental | Simulated | |
| 1 | WAlSiN | 940 | 872 | 0.00128 |
| 2 | SiON | 445 | 407 | 0.00371 |
| 3 | $SiO_2$ | 440 | 430 | 0.00377 |
| 4 | W/WAlSiN/SiON/$SiO_2$ | 280/85/70/30 | 250/78/68/37 | 0.0002270 |
| 5 | W/WAlSiN/Intermixed layer/SiON/$SiO_2$ | 280/85/70/30 | 250/80/5/70/40 | 0.0002042 |

The effective optical constants of WAlSiN layer and optical constants of SiON and $SiO_2$ anti-reflection layers calculated are considered for simulation studies of the multilayer stack. In the multilayer stack, the simulation indicates an excellent fit with a deviation in fitting of 0.0002042 between the experimental and simulated spectra. Moreover, the thickness of individual layers in the multilayer stack after fitting shows a slight variation from the measured thickness of the film (as tabulated in Table 2), as this variation of thickness is due to the measured optical constants. However, at the interface of WAlSiN and SiON layer there exists a thin intermixed layer of ~5 nm in the multilayer stack, which is known from the spectroscopic ellipsometry measurement. The influences of the intermixed layer on reflectance spectra are simulated with respect to the measured reflectance spectra and the same is shown in Figure 11. The schematics of multilayer stack with simulated thicknesses are incorporated as in-sets in Figure 11a,b. The simulated spectrum without the presence of intermixed layer depicts a small hump in the wavelength range of 600–1200 nm and two reflectance minima at 712 and 1305 nm, as indicated in Figure 11a. The simulated thicknesses for the individual layers are labelled in the schematic (inset) of Figure 11a and are tabulated in Table 2. Figure 11b shows the simulated and the experimental reflectance spectra of multilayer stack in which the presence of the intermediate layer between WAlSiN main absorber layer and SiON layer exhibits an excellent fit. After introducing the intermixed layer, the reflectance minimum shifts from 712 nm to 637 nm, thereby implies better absorptance property of the multilayer stack, as marked in Figure 11b. However, the reflectance minimum at 1305 nm does not shift but the overall reflectance in the wavelength range of 600–1300 nm is less than 1%. Furthermore, the gradual change in the refractive index of the multilayer stack due to intermixed layer ensures the near-zero reflectance, i.e., W/WAlSiN/intermixedlayer/SiON/$SiO_2$ (3.83/2.52/2.28/1.56/1.51 @ 550 nm) from the top anti-reflection layer to the bottom of the substrate. This comparison of simulated spectra with and without intermixed layer confirms that due the formation of the intermixed layer in between WAlSiN and SiON layers, the reflectance decreases in the wavelength range of 600–1200 nm. So, the intermixing at the interface favors in lowering the reflectance by a gradual change in the optical constants. Similar, intermixing is also observed at the interface of WAlN and WAlON in W/WAlN/WAlON/$Al_2O_3$ solar selective coating [18]. Zhao et al. reported the optimized three-layer solar absorber coating using CODE simulation tool, which exhibits a high solar absorptance of 0.97 and low thermal emissivity [60]. Their simulated results were in good agreement with the experimental data, which indicates the reliability of the approach through computational simulation.

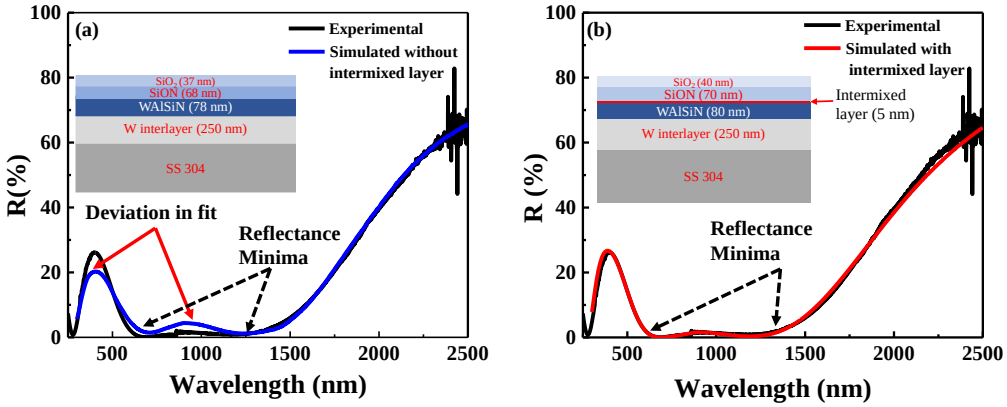


**Figure 11.** The multilayer reflectance spectra of the solar absorber fitted with simulated spectra generated from simulation: (**a**) Without the intermixed layer and (**b**) with the intermixed layer. The schematics of the multi-layer stack with simulated layer thicknesses are presented as insets.

## 4. Conclusions

We report the detailed evaluation and analysis of enhanced spectrally selective solar absorber coating of W/WAlSiN/SiON/$SiO_2$ by means of spectroscopic ellipsometry. The optical constants of individual layers and multilayer stack were obtained by curve fitting the ψ and Δ plots using appropriate dispersion models. The Cauchy absorbent dispersion model was used for main absorber layer (WAlSiN), Tauc-Lorentz model for anti-reflection layers (SiON and $SiO_2$) and Bruggeman effective medium approximation for the intermixed layer formed in between WAlSiN and SiON layers. The obtained optical constants depict a gradation in the designed multilayer stack from top anti-reflection layer to substrate due to which an enhanced solar absorption is achieved. The multilayer stack of W/WAlSiN/SiON/$SiO_2$ (280/85/70/30 nm) deposited on SS substrate exhibits a high solar absorptance of 0.955 and low thermal emissivity of 0.10. Furthermore, the wide-angle selectivity of the multilayer stack was measured by varying the incident angle (8°–68°) and the multilayer stack exhibits an excellent wide-angle selectivity up to 58°. The optical simulated spectra of individual layers and multilayer stack using software shows a good correlation between the measured and experimental spectra. The simulation results based on optical constants of multilayer stack measured using ellipsometry describe the influence of intermixed layer in achieving high solar absorptance.

**Author Contributions:** Conceptualization, H.C.B.; methodology, K.N.; software, K.N. and P.K.; validation, K.N., P.K., and A.B.; formal analysis, V.P.K. and G.S.; investigation, K.N.; resources, H.C.B.; data curation, K.N. and A.B.; writing—original draft preparation, K.N; writing—review and editing, H.C.B.; visualization, H.C.B. and K.N.; supervision, H.C.B.; project ad-ministration, H.C.B.; funding acquisition, H.C.B. All authors have read and agreed to the published version of the manuscript.

**Funding:** This research was funded by Department of Science and Technology (DST), grant number DST (U-1-144) and Centre Franco-Indien pour la Promotion de la Recherche Avancée (CEFIPRA), grant number (U-1-154).

**Acknowledgments:** The authors thank Siju John for FESEM measurement measurements. We thank the Department of Science and Technology, DST (U-1-144) and Centre Franco-Indien pour la Promotion de la Recherche Avancée, CEFIPRA (U-1-154) for providing funding support. K. Niranjan thanks CSIR for providing CSIR-SRF fellowship.

**Conflicts of Interest:** All authors declare no conflict of interest.

## References

1. Weinstein, L.A.; Loomis, J.; Bhatia, B.S.; Bierman, D.M.; Wang, E.N.; Chen, G. Concentrating solar power. *Chem. Rev.* **2015**, *115*, 12797–12838. [CrossRef]
2. Kennedy, C.E. *Review of Mid-to High-Temperature Solar Selective Absorber Materials*; No. NREL/TP-520-31267; National Renewable Energy Lab.: Golden, CO, USA, July 2002.

3. Zhang, Q.-C. Recent progress in high-temperature solar selective coatings. *Sol. Energy Mater. Sol. Cells* **2000**, *62*, 63–74. [CrossRef]
4. Selvakumar, N.; Barshilia, H.C. Review of physical vapor deposited (PVD) spectrally selective coatings for mid-and high-temperature solar thermal applications. *Sol. Energy Mater. Sol. Cells* **2012**, *98*, 1–23. [CrossRef]
5. Xu, K.; Du, M.; Hao, L.; Mi, J.; Yu, Q.; Li, S. A review of high-temperature selective absorbing coatings for solar thermal applications. *J. Mater.* **2020**, *6*, 167–182. [CrossRef]
6. Cao, F.; Kraemer, D.; Sun, T.; Lan, Y.; Chen, G.; Ren, Z. Enhanced thermal stability of W-Ni-Al2O3Cermet-based spectrally selective solar absorbers with tungsten infrared reflectors. *Adv. Energy Mater.* **2015**, *5*, 1401042. [CrossRef]
7. Sibin, K.; John, S.; Barshilia, H.C. Control of thermal emittance of stainless steel using sputtered tungsten thin films for solar thermal power applications. *Sol. Energy Mater. Sol. Cells* **2015**, *133*, 1–7. [CrossRef]
8. Ibrahim, K.; A Taha, H.; Rahman, M.M.; Kabir, H.; Jiang, Z.-T. Solar selective performance of metal nitride/oxynitride based magnetron sputtered thin film coatings: A comprehensive review. *J. Opt.* **2018**, *20*, 033001. [CrossRef]
9. Kanda, H.; Uzum, A.; Harano, N.; Yoshinaga, S.; Ishikawa, Y.; Uraoka, Y.; Fukui, H.; Harada, T.; Ito, S. $Al_2O_3/TiO_2$ double layer anti-reflection coating film for crystalline silicon solar cells formed by spray pyrolysis. *Energy Sci. Eng.* **2016**, *4*, 269–276. [CrossRef]
10. Kim, J.; Park, J.; Hong, J.H.; Choi, S.J.; Kang, G.H.; Yu, G.J.; Kim, N.S.; Song, H.-E. Double antireflection coating layer with silicon nitride and silicon oxide for crystalline silicon solar cell. *J. Electroceram.* **2012**, *30*, 41–45. [CrossRef]
11. Rebouta, L.; Sousa, A.; Andritschky, M.; Cerqueira, F.; Tavares, C.; Santilli, P.; Pischow, K. Solar selective absorbing coatings based on AlSiN/AlSiON/$AlSiO_y$ layers. *Appl. Surf. Sci.* **2015**, *356*, 203–212. [CrossRef]
12. Barshilia, H.C.; Selvakumar, N.; Rajam, K.; Biswas, A. Spectrally selective NbAlN/NbAlON/Si3N4 tandem absorber for high-temperature solar applications. *Sol. Energy Mater. Sol. Cells* **2008**, *92*, 495–504. [CrossRef]
13. Bilokur, M.; Gentle, A.; Arnold, M.D.; Cortie, M.B.; Smith, G.B. Spectrally selective solar absorbers based on Ta:$SiO_2$ Cermets for next-generation concentrated solar-thermal applications. *Energy Technol.* **2020**, *8*, 2000125. [CrossRef]
14. Snyder, P.G.; Xiong, Y.; Woollam, J.A.; Al-Jumaily, G.A.; Gagliardi, F.J. Graded refractive index silicon oxynitride thin film characterized by spectroscopic ellipsometry. *J. Vac. Sci. Technol. A* **1992**, *10*, 1462–1466. [CrossRef]
15. Al-Rjoub, A.; Rebouta, L.; Costa, P.; Barradas, N.; Alves, E.; Ferreira, P.; Abderrafi, K.; Matilainen, A.; Pischow, K. A design of selective solar absorber for high temperature applications. *Sol. Energy* **2018**, *172*, 177–183. [CrossRef]
16. Barshilia, H.C.; Selvakumar, N.; Rajam, K.S.; Rao, D.V.S.; Muraleedharan, K.; Biswas, A. TiAlN/TiAlON/Si3N4 tandem absorber for high temperature solar selective applications. *Appl. Phys. Lett.* **2006**, *89*, 191909. [CrossRef]
17. Biswas, A.; Bhattacharyya, D.; Barshilia, H.; Selvakumar, N.; Rajam, K. Spectroscopic ellipsometric characterization of TiAlN/TiAlON/Si3N4 tandem absorber for solar selective applications. *Appl. Surf. Sci.* **2008**, *254*, 1694–1699. [CrossRef]
18. Dan, A.; Biswas, A.; Sarkar, P.; Kashyap, S.; Chattopadhyay, K.; Barshilia, H.C.; Basu, B. Enhancing spectrally selective response of W/WAlN/WAlON/Al2O3-based nanostructured multilayer absorber coating through graded optical constants. *Sol. Energy Mater. Sol. Cells* **2018**, *176*, 157–166. [CrossRef]
19. Al-Rjoub, A.; Rebouta, L.; Costa, P.; Vieira, L. Multi-layer solar selective absorber coatings based on W/WSiAlNx /WSiAlOyNx/SiAlOx for high temperature applications. *Sol. Energy Mater. Sol. Cells* **2018**, *186*, 300–308. [CrossRef]
20. Escobar-Galindo, R.; Guillén, E.; Heras, I.; Rincón-Llorente, G.; Alcón-Camas, M.; Lungwitz, F.; Munnik, F.; Schumann, E.; Azkona, I.; Krause, M. Design of high-temperature solar-selective coatings based on aluminium titanium oxynitrides AlyTi1-y(OxN1-x). Part 2: Experimental validation and durability tests at high temperature. *Sol. Energy Mater. Sol. Cells* **2018**, *185*, 183–191. [CrossRef]
21. Wang, X.; Luo, T.; Li, Q.; Cheng, X.; Li, K. High performance aperiodic metal-dielectric multilayer stacks for solar energy thermal conversion. *Sol. Energy Mater. Sol. Cells* **2019**, *191*, 372–380. [CrossRef]
22. Valleti, K.; Krishna, D.M.; Joshi, S. Functional multi-layer nitride coatings for high temperature solar selective applications. *Sol. Energy Mater. Sol. Cells* **2014**, *121*, 14–21. [CrossRef]
23. Liu, Y.; Wu, Z.; Yin, L.; Zhang, Z.; Wu, X.; Wei, D.; Zhang, Q.; Cao, F. High-temperature air-stable solar absorbing coatings based on the cermet of MoSi2 embedded in SiO2. *Sol. Energy Mater. Sol. Cells* **2019**, *200*, 109946. [CrossRef]
24. Zou, C.; Xie, W.; Shao, L. Functional multi-layer solar spectral selective absorbing coatings of AlCrSiN/AlCrSiON/AlCrO for high temperature applications. *Sol. Energy Mater. Sol. Cells* **2016**, *153*, 9–17. [CrossRef]
25. Song, P.; Wu, Y.; Wang, L.; Sun, Y.; Ning, Y.; Zhang, Y.; Dai, B.; Tomasella, E.; Bousquet, A.; Wang, C. The investigation of thermal stability of Al/NbMoN/NbMoON/SiO2 solar selective absorbing coating. *Sol. Energy Mater. Sol. Cells* **2017**, *171*, 253–257. [CrossRef]
26. Yang, D.; Zhao, X.; Liu, Y.; Li, J.; Liu, H.; Hu, X.; Li, Z.; Zhang, J.; Guo, J.; Chen, Y.; et al. Enhanced thermal stability of solar selective absorber based on nano-multilayered AlCrSiO films. *Sol. Energy Mater. Sol. Cells* **2020**, *207*, 110331. [CrossRef]
27. Al-Rjoub, A.; Rebouta, L.; Cunha, N.; Fernandes, F.; Barradas, N.; Alves, E. W/AlSiTiNx/SiAlTiOyNx/SiAlOx multilayered solar thermal selective absorber coating. *Sol. Energy* **2020**, *207*, 192–198. [CrossRef]
28. Niranjan, K.; Kondaiah, P.; Srinivas, G.; Barshilia, H.C. Optimization of W/WAlSiN/SiON/SiO2 tandem absorber consisting of double layer anti-reflection coating with broadband absorption in the solar spectrum region. *Appl. Surf. Sci.* **2019**, *496*, 143651. [CrossRef]

29. Niranjan, K.; Soum-Glaude, A.; Carling-Plaza, A.; Bysakh, S.; John, S.; Barshilia, H.C. Extremely high temperature stable nanometric scale multilayer spectrally selective absorber coating: Emissivity measurements at elevated temperatures and a comprehensive study on ageing mechanism. *Sol. Energy Mater. Sol. Cells* **2021**, *221*, 110905. [CrossRef]
30. Manikandan, G.; Iniyan, S.; Goic, R. Enhancing the optical and thermal efficiency of a parabolic trough collector—A review. *Appl. Energy* **2019**, *235*, 1524–1540. [CrossRef]
31. *SCOUT Thin Film Analysis Software Handbook*; W Theiss Hard and Software: Aachen, Germany, 2017.
32. Meziani, S.; Moussi, A.; Mahiou, L.; Outemzabet, R. Effect of thermal annealing on double anti reflection coating SiNx/SiO2. In Proceedings of the 2015 3rd International Renewable and Sustainable Energy Conference (IRSEC), Marrakech, Morocco, 10–13 December 2015; pp. 1–5.
33. He, X.; Li, Y.; Wang, L.; Sun, Y.; Zhang, S. High emissivity coatings for high temperature application: Progress and prospect. *Thin Solid Films* **2009**, *517*, 5120–5129. [CrossRef]
34. Hu, R.; Song, J.; Liu, Y.; Xi, W.; Zhao, Y.; Yu, X.; Cheng, Q.; Tao, G.; Luo, X. Machine learning-optimized Tamm emitter for high-performance thermophotovoltaic system with detailed balance analysis. *Nano Energy* **2020**, *72*, 104687. [CrossRef]
35. Xi, W.; Liu, Y.; Song, J.; Hu, R.; Luo, X. High-throughput screening of a high-Q mid-infrared Tamm emitter by material informatics. *Opt. Lett.* **2021**, *46*, 888–891. [CrossRef] [PubMed]
36. Raut, H.K.; Ganesh, V.A.; Nair, A.S.; Ramakrishna, S. Anti-reflective coatings: A critical, in-depth review. *Energy Environ. Sci.* **2011**, *4*, 3779–3804. [CrossRef]
37. Cao, L.; Sendur, K. Surface roughness effects on the broadband reflection for refractory metals and polar dielectrics. *Materials* **2019**, *12*, 3090. [CrossRef]
38. Wen, C.-D.; Mudawar, I. Modeling the effects of surface roughness on the emissivity of aluminum alloys. *Int. J. Heat Mass Transf.* **2006**, *49*, 4279–4289. [CrossRef]
39. Liu, Y.; Song, J.; Zhao, W.; Ren, X.; Cheng, Q.; Luo, X.; Fang, N.X.; Hu, R. Dynamic thermal camouflage via a liquid-crystal-based radiative metasurface. *Nanophotonics* **2020**, *9*, 855–863. [CrossRef]
40. Song, J.; Huang, S.; Ma, Y.; Cheng, Q.; Hu, R.; Luo, X. Radiative metasurface for thermal camouflage, illusion and messaging. *Opt. Express* **2020**, *28*, 875–885. [CrossRef] [PubMed]
41. Fujiwara, H. *Spectroscopic Ellipsometry: Principles and Applications*; John Wiley & Sons, Ltd.: Chichester, England, 2007.
42. Knopp, K.J.; Mirin, R.P.; Bertness, K.A.; Silverman, K.L.; Christensen, D.H. Compound semiconductor oxide antireflection coatings. *J. Appl. Phys.* **2000**, *87*, 7169–7175. [CrossRef]
43. Hilfiker, J.N.; Singh, N.; Tiwald, T.; Convey, D.; Smith, S.M.; Baker, J.H.; Tompkins, H.G. Survey of methods to characterize thin absorbing films with spectroscopic ellipsometry. *Thin Solid Films* **2008**, *516*, 7979–7989. [CrossRef]
44. Jellison, G.E., Jr.; Modine, F.A. Parameterization of the optical functions of amorphous materials in the interband region. *Appl. Phys. Lett.* **1996**, *69*, 371–373. [CrossRef]
45. Jellison, J.G.; Modine, F.; Doshi, P.; Rohatgi, A. Spectroscopic ellipsometry characterization of thin-film silicon nitride. *Thin Solid Films* **1998**, *313-314*, 193–197. [CrossRef]
46. Jellison, J.G. Spectroscopic ellipsometry data analysis: Measured versus calculated quantities. *Thin Solid Films* **1998**, *313–314*, 33–39. [CrossRef]
47. Wemple, S.H. Refractive-index behavior of amorphous semiconductors and glasses. *Phys. Rev. B* **1973**, *7*, 3767–3777. [CrossRef]
48. Ma, H.-P.; Lu, H.-L.; Yang, J.-H.; Li, X.-X.; Wang, T.; Huang, W.; Yuan, G.-J.; Komarov, F.F.; Zhang, D.W. Measurements of microstructural, chemical, optical, and electrical properties of silicon-oxygen-nitrogen films prepared by plasma-enhanced atomic layer deposition. *Nanomaterials* **2018**, *8*, 1008. [CrossRef]
49. Ordal, M.A.; Long, L.L.; Bell, R.J.; Bell, S.E.; Alexander, R.W.; Ward, C.A. Optical properties of the metals Al, Co, Cu, Au, Fe, Pb, Ni, Pd, Pt, Ag, Ti, and W in the infrared and far infrared. *Appl. Opt.* **1983**, *22*, 1099–1119. [CrossRef]
50. Sancho-Parramon, J.; Janicki, V.; Zorc, H. On the dielectric function tuning of random metal-dielectric nanocomposites for metamaterial applications. *Opt. Express* **2010**, *18*, 26915–26928. [CrossRef] [PubMed]
51. Heras, I.; Krause, M.; Abrasonis, G.; Pardo, A.; Endrino, J.; Guillén, E.; Escobar-Galindo, R. Advanced characterization and optical simulation for the design of solar selective coatings based on carbon: Transition metal carbide nanocomposites. *Sol. Energy Mater. Sol. Cells* **2016**, *157*, 580–590. [CrossRef]
52. Keçebaş, M.A.; Şendur, K. Enhancing the spectral reflectance of refractory metals by multilayer optical thin-film coatings. *J. Opt. Soc. Am. B* **2018**, *35*, 1845–1853. [CrossRef]
53. Ji, D.; Song, H.; Zeng, X.; Hu, H.; Liu, K.; Zhang, N.; Gan, Q. Broadband absorption engineering of hyperbolic metafilm patterns. *Sci. Rep.* **2015**, *4*, 4498. [CrossRef] [PubMed]
54. Joly, M.; Antonetti, Y.; Python, M.; Lazo, M.G.; Gascou, T.; Hessler-Wyser, A.; Scartezzini, J.-L.; Schüler, A. Selective solar absorber coatings on receiver tubes for CSP—Energy-efficient production process by sol-gel dip-coating and subsequent induction heating. *Energy Procedia* **2014**, *57*, 487–496. [CrossRef]
55. Rebouta, L.; Capela, P.; Andritschky, M.; Matilainen, A.; Santilli, P.; Pischow, K.; Alves, E. Characterization of TiAlSiN/TiAlSiON/SiO2 optical stack designed by modelling calculations for solar selective applications. *Sol. Energy Mater. Sol. Cells* **2012**, *105*, 202–207. [CrossRef]
56. Soum-Glaude, A.; Di Giacomo, L.; Quoizola, S.; Laurent, T.; Flamant, G. Selective surfaces for solar thermal energy conversion in CSP: From multilayers to nanocomposites. *Nanotechnol. Energy Sustain.* **2017**, 231–248. [CrossRef]

57. Li, M.; Zeng, L.; Chen, Y.; Zhuang, L.; Wang, X.; Shen, H. Realization of colored multicrystalline silicon solar cells with SiO2/SiNx:H double layer antireflection coatings. *Int. J. Photoenergy* **2013**, *2013*, 352473. [CrossRef]
58. Zhang, J.; Chen, T.; Liu, Y.; Liu, Z.; Yang, H. Modeling of a selective solar absorber thin film structure based on double TiNxOy layers for concentrated solar power applications. *Sol. Energy* **2017**, *142*, 33–38. [CrossRef]
59. Zheng, L.; Zhou, F.; Zhou, Z.; Song, X.; Dong, G.; Wang, M.; Diao, X. Angular solar absorptance and thermal stability of Mo–$SiO_2$ double cermet solar selective absorber coating. *Sol. Energy* **2015**, *115*, 341–346. [CrossRef]
60. Zhao, S.; Wäckelgård, E. Optimization of solar absorbing three-layer coatings. *Sol. Energy Mater. Sol. Cells* **2006**, *90*, 243–261. [CrossRef]